Accepted (peer-reviewed) version

This document is the Accepted Manuscript version of a Published Work that appeared in final form in *ACS Appl. Mater. Interface* (Volume 15, Issue 23; Date of publication: June 1, 2023), copyright © American Chemical Society after peer review and technical editing by the publisher. To access the final edited and published work see

https://pubs.acs.org/doi/abs/10.1021/acsami.3c03366

Mixed organic cations promote ambient light-induced formation of metallic lead in lead halide perovskite crystals

Aniruddha Ray,[1,2] Beatriz Martín-García,[1,3,4] Mirko Prato,[1] Anna Moliterni,[5] Simone Bordignon,[6] Davide Spirito,[7] Sergio Marras,[1] Luca Goldoni,[1] Karunakara Moorthy Boopathi,[1] Fabrizio Moro,[8] Nicola Pietro Maria Casati,[9] Carlotta Giacobbe,[10] Makhsud I. Saidaminov,[11] Cinzia Giannini,[5] Michele R. Chierotti,[6] Roman Krahne,[1] Liberato Manna,[1,*] Ahmed L. Abdelhady[1,12, 13*]

[1]Istituto Italiano di Tecnologia, Via Morego 30, 16163 Genova, Italy

[2]RGS Development B.V. Bijlestaal 54a, Broek op Langedijk 1721 PW, Dijk en Waard, Netherlands

[3]CIC nanoGUNE, Tolosa Hiribidea, 76, 20018 Donostia-San Sebastian, Spain

[4]IKERBASQUE, Basque Foundation for Science, 48009 Bilbao, Spain

[5]Istituto di Cristallografia, Consiglio Nazionale delle Ricerche, Via Amendola 122/O, 70126 Bari, Italy

[6]Department of Chemistry, University of Torino, 10125 Torino, Italy

[7]IHP—Leibniz-Institut für innovative Mikroelektronik, Im Technologiepark 25, D-15236 Frankfurt (Oder), Germany

[8]Dipartimento di Scienza dei Materiali, Università degli Studi Milano-Bicocca, Milano 20125, Italy

[9]Laboratory for Synchrotron Radiation—Condensed Matter, Paul Scherrer Institut, 5232 Villigen, Switzerland

[10]European Synchrotron Radiation Facility, 71 Avenue Des Martyrs, Grenoble 38040, France

[11]Department of Chemistry, University of Victoria, Victoria, British Columbia V8P 5C2, Canada

[12]Department of Chemistry Khalifa University P.O. Box 127788, Abu Dhabi, United Arab Emirates

[13]Advanced Materials Chemistry Center (AMCC) Khalifa University P.O. Box 127788, Abu Dhabi, United Arab Emirates

∗Corresponding author: liberato.manna@iit.it and ahmed.abdelhady@ku.ac.ae

Abstract

One major concern towards the performance and stability of halide perovskite-based optoelectronic devices is the formation of metallic lead that promotes nonradiative recombination of charge carriers. The origin of metallic lead formation is being disputed whether it occurs during the perovskite synthesis or only after light, electron or X-ray beam irradiation, or thermal annealing. Here we show that the quantity of metallic lead detected in perovskite crystals depends on the concentration and composition of the precursor solution. Through a controlled crystallization process, we grew black-colored mixed dimethylammonium (DMA)/methylammonium (MA) lead tribromide crystals. The black color is suggested to be due to the presence of small lead clusters. Despite the unexpected black coloring, the crystals show higher crystallinity and less defect density with respect to the standard yellow-colored DMA/$MAPbBr_3$ crystals, as indicated by X-ray rocking curve and dark current measurements, respectively. While the formation of metallic lead could still be induced by external factors, the

precursor solution composition and concentration can facilitate the formation of metallic lead during the crystallization process. Our results indicate that additional research is required to fully understand the perovskite precursor solution chemistry.

Keywords: perovskites, single crystals, crystallization, light-induced, metallic lead

Introduction

Hybrid lead halide perovskites ($APbX_3$: where A = methylammonium/formamidinium, X = halogen ion) have demonstrated high potential as active layers in different optoelectronic devices including solar cells[1] and light-emitting diodes (LEDs).[2] This is due to their exceptional properties including high defect tolerance, high charge carrier diffusion length, and their tunable bandgap. Nevertheless, lead halide perovskites do still suffer from some limitations. One major concern is the formation of metallic lead, which acts as a recombination center limiting the performance of solar cells[3–5] and LEDs.[6–8] So far, it is still debated whether Pb(0) forms during perovskite crystallization and growth, or only after light or X-ray irradiation, or thermal annealing.[9]

Here we demonstrate the growth of unusual black-colored lead bromide-based perovskite crystals. We found that the blackening happens under certain chemical conditions,

including excess $PbBr_2$ in the precursor solution, using mixed A-site cations, namely methylammonium (MA) and dimethylammonium (DMA), and performing the crystallization under ambient light. We propose that the black color is due to the formation of metallic lead. Interestingly, the black-colored crystals of DMA/$MAPbBr_3$ remain black and shiny upon cleaving, however they turn yellow when they are ground into powder. The as-grown black-colored crystals and their powders are of a higher crystalline quality compared to the standard yellow-colored DMA/$MAPbBr_3$ crystals and their powders, as indicated by X-ray rocking curve and synchrotron X-ray powder diffraction (SXRPD) measurements. A crystallographic study by SXRPD proved that the crystal structure of both samples is strongly similar. The higher quality of these black-colored crystals with respect to the yellow-colored DMA/$MAPbBr_3$ crystals is further confirmed by their lower defect density, as suggested by their lower dark current. ^{207}Pb Solid-state nuclear magnetic resonance revealed that the local Pb environment in the two samples (yellow- and black-colored crystals) is different. Both photoluminescence measurements and photodetector spectral response measurements indicate that the black coloring is not due to a change in the perovskite bandgap, as the black-colored crystals emit and detect light in a very similar wavelength range as the yellow-colored crystals. Our results indicate that the perovskite precursor solution and crystallization conditions play a critical role in the formation of the undesired metallic lead.

Experimental

Materials: *N*-methylformamide (NMF, 99.9%), *N*,*N*-dimethylformamide (DMF, 99.9%), hydrobromic acid (HBr, 48 wt% in water), dichloromethane (DCM, 99.8%) and lead bromide ($PbBr_2$, 99%) were purchased and used as received from Sigma-Aldrich.

Mixed A-site cation crystal growth: mixed dimethylammonium/methylammonium lead tribromide ($DMA/MAPbBr_3$) crystals were grown from a 0.4 M $PbBr_2$ (for the yellow-colored crystals) and 1.2 M (for the black-colored crystals) solution in a mixture of DMF, NMF, and HBr (4.05:1.5:1 by volume). 1 mL of the respective precursor solutions was transferred in an 8 mL vial and the entire setup was sealed with aluminum foil. This was subsequently inserted into a larger 40 mL vial that contains 7.5 mL of DCM. Piercing a hole in the aluminum foil allowed the crystallization to begin due to the volatile DCM. All steps were performed at room temperature. The crystals were collected after 3 to 4 days and wiped on a filter paper before they were dried for a period of 24 h in a vacuum oven that was maintained at 40 °C.

Crystal characterization:

Liquid-state proton nuclear magnetic resonance: ^{1}H NMR spectrum was acquired at a temperature of 300 K, using a Bruker Avance III 400 MHz spectrometer, supplied with a Broad Band Inverse probe. After the 90-degree excitation pulse optimization,[10] 16 transients were collected without steady state scans. The acquisition time and the inter pulses delay were 4 and 50 s, respectively. The spectral width was 20.55 ppm with the offset at 6.18 ppm, and receiver was fixed (64). An exponential function corresponding to 0.3 Hz was used to smooth the noise, prior to the Fourier transform applied to the Free Induction Decay (FID). The spectrum was

manually phased, automatically baseline adjusted, and referred to the residual of non-deuterated dimethyl sulfoxide (DMSO) signal set at 2.50 ppm.

Energy dispersive X-ray spectroscopy (EDS) was conducted using a JEOL JSM-7500FA SEM-Analytical field-emission scanning electron microscopy (SEM) with an Oxford X-Max 80 system that is equipped with an 80 mm^2 silicon drift detector (SDD).

X-ray photoelectron spectroscopy (XPS) measurements were performed using a Kratos Axis Ultra^{DLD} spectrometer, with a monochromatic Al Kα source (15 kV, 20 mA). The spectra were taken on a 300 × 700 μm^2 area. Wide scans were collected with an energy step of 1 eV and a constant pass energy of 160 eV, and the high-resolution spectra were acquired at an energy step of 0.1 eV and a constant pass energy of 10 eV. The C 1s peak at 284.8 eV was used as a reference to the binding energy scale. The spectra were analyzed using the CasaXPS software (version 2.3.24).

*Electron paramagnetic resonance (EPR) measurements. S*amples were prepared inside a glovebox and then were loaded into a suprasil EPR quartz tube that was sealed with a tip-off manifold. CW-EPR spectra were recorded at room temperature using a Varian spectrometer that is coupled to a Bruker super-High Q cavity (ER4122SHQE) and a liquid helium flow cryostat. Experimental parameters were modulation frequency: 100 kHz, microwave power 5 – 10 mW, and modulation amplitude 5 Gauss.

Laboratory X-ray powder diffraction (LXRPD) was performed at room temperature using a PANalytical Empyrean X-ray diffractometer on the as-grown crystals and on the ground crystals.

The X-ray diffractometer is equipped with a 1.8 kW Cu Kα ceramic X-ray tube and a PIXcel3D 2 × 2 area detector that operates at 45 kV and 40 mA. HighScore 4.1 software from PANanalytical[11] was used to analyze the LXRPD data. A 0.013° step size and 0.013°/s scan speed were maintained for all measurements.

X-ray rocking curves analysis was performed on a Rigaku SmartLab diffractometer, equipped with 9kW CuKα rotating anode, parallel mirror (PM), RxRy double tilt stage and SC-70 scintillation counter (0D detector).

Temperature-dependent synchrotron X-ray powder diffraction (SXRPD) was performed at the Materials Science beamline of the Swiss Light Source,[12] on sealed capillaries in transmission geometry and using a cryostream nitrogen blower and Mythen III detector. A 4 mm-wide beam with a wavelength of 0.4923 Å calibrated against an NIST Si standard (SRM-640d) was employed.

Micro-Raman spectroscopy measurements were carried out using Renishaw inVia instrument, and 633 nm laser as excitation source (power < 1 mW to avoid damage of the samples). In this way, we worked under non-resonant conditions to avoid signal contribution from the photoluminescence of the samples. In the case of room-temperature measurements, we used a 10× objective (0.25 N.A.) and collected data from 5-7 points for at least two crystals synthetized in different batches. To perform temperature-dependent micro-Raman measurements, we used a liquid N_2 cryostat (Linkam) mounted in the piezo XYZ stage of the Raman instrument and an objective (20×, 0.40 NA, long working distance). We checked each sample by collecting and analyzing Raman data from 5 different points.

Solid-state NMR (SSNMR) spectra were recorded using a Bruker Avance II 400 Ultra Shield instrument, which was operating at 400.23 MHz (^{1}H nuclei), 100.63 MHz (^{13}C nuclei), and 83.73 MHz (^{207}Pb nuclei). Samples were placed into cylindrical zirconia rotors having a 4 mm outer diameter and a volume of 80 μL. A certain amount of each sample was used to fill the rotor in the case of ground powders, or were mixed with KI (potassium iodide) in the case of crystals, to ensure a proper filling of the rotor for achieving stability in its rotation.

^{13}C CPMAS spectra were acquired using a spinning speed of 12 kHz, and a ramp cross-polarization pulse sequence with a contact time of 3 ms, a 90° ^{1}H pulse of 3.60 μs, and optimized recycle delays between 80 and 92.5 s (equal to $5 \cdot T_1$). The number of scans was in the range of 900-2000, depending on the sample. A two-pulse phase modulation (TPPM) decoupling scheme with a radiofrequency field of 69.4 kHz was used for every ^{13}C CPMAS spectrum.

^{1}H MAS spectra was acquired using a spinning speed of 12 kHz, and a 90° ^{1}H pulse of 3.60 μs, a recycle delay of 1 s, for 1 transient, employing 67 Hz of spectral resolution.

^{207}Pb MAS spectra were acquired using 10 kHz spinning speed with the DEPTH sequence (π/2–π–π) for the suppression of the probe background signal (^{207}Pb 90° = 3.0 μs; relaxation delay of 15 s; 2000–15000 scans).

The ^{13}C chemical shift scale was calibrated by the methylenic signal of external standard glycine (at 43.7 ppm with respect to TMS - tetramethylsilane); the ^{1}H scale was calibrated through using adamantane (^{1}H signal at 1.87 ppm with respect to TMS) as external standard; the ^{207}Pb scale was calibrated through the signal of $Pb(NO_3)_2$ (-3491 ppm with respect to $Pb(CH_3)_4$) as external standard.

Absorbance measurements for the ground crystals and the as-grown crystals were performed on a Cary 5000 spectrometer that is equipped with a diffuse reflectance accessory as well as an integrating sphere for transmission measurements.

Micro-photoluminescence (μ-PL) measurements were performed with a Renishaw inVia 1000 micro-Raman instrument using a 457 nm laser as excitation source and a 50× objective, collecting the Raman signal in 5 points for each sample. For checking the reproducibility among samples from different batches, we characterized at least three crystals and their corresponding powders.

Temperature-dependent steady-state PL measurements were performed on a FLS920 fluorescence spectrometer (Edinburgh instruments) equipped with optical fibers to collect the PL signal from the samples placed inside a closed-cycle helium cryostat (Advanced Research Systems, Inc.). Note that, the samples were attached to a sapphire substrate (TedPella®) using Ag paste. As an excitation source, a 445 nm continuous wave (CW) Oxxius laser in a reflecting geometry (45° between excitation and emission) was used and PL spectra were collected every 10 K.

Electrical characterization was performed through depositing 60 nm Au contacts on opposite sides of the crystals, using a shadow mask with 1 × 1 mm (length and width) apertures, at a rate of 0.6 Å/s (Kenosistec® e-beam evaporator with a cooling system for sample holder). For spectral responsivity, a Xe lamp coupled to a Spectral Products CM110 monochromator was used.

Results and Discussion

Solvent acidolysis crystallization (SAC) was used to grow mm-sized crystals by modifying the original recipe that we previously reported for $MAPbX_3$,[13,14] MA_2CuX_4,[15] and recently for the typical yellow-colored mixed DMA/$MAPbBr_3$ crystals.[16] The SAC process depends on the *in-situ* formation of the organic A-site cation through the acidolysis of the corresponding amide. For instance, the *in-situ* formation of the MA cation is a result of the hydrolysis of *N*-methylformamide in the presence of an acid. Here, we grew black-colored DMA/$MAPbBr_3$ crystals (Figure 1) through controlling the $PbBr_2$ concentration. Our previously reported "Yellow" DMA/$MAPbBr_3$ crystals were grown under low $PbBr_2$ concentration (0.4 M) (Figure 1a),[16] while the "Black" DMA/$MAPbBr_3$ crystals in this work were synthesized under a higher $PbBr_2$ concentration of 1.2 M (Figure 1b). Note that in both cases the growth conditions are considered to be Br-rich due to the addition of HBr in the feed solution. The Black crystals grown from the concentrated $PbBr_2$ solution were obtained regardless of the purity of the used $PbBr_2$ salt; both 98% and 99.999% $PbBr_2$ resulted in black-colored crystals. Other than the required high $PbBr_2$ concentration (1.2 M), we observed that a 2.5:1 *N*,*N*-dimethylformamide (DMF):*N*-methylformamide (NMF) ratio in the feed solution, similar to what we used to grow the Yellow crystals, is another requirement to achieve fully black-colored three-dimensional (3D) perovskite crystals. Using 1.2 M $PbBr_2$ in only DMF or only NMF formed the typical white non-perovskite $DMAPbBr_3$ and the orange perovskite $MAPbBr_3$, respectively, without any black coloration. On the other hand, a 5:1 DMF:NMF resulted in black-colored but mixed-phase crystals, and a 1.25:1 ratio led to the formation of orange-colored crystals with black cores. See Figure S1 in the Supporting Information for laboratory XRD patterns and photographs of the crystals grown from different DMF:NMF ratios. In addition to the $PbBr_2$ concentration and DMF:NMF ratio, we found

that light plays a critical role in the black coloring. Performing the crystallization in a dark environment, even by using the higher $PbBr_2$ concentration (1.2 M), did not lead to any blackening (Figure 1c), hence suggesting a photo-induced chemical change. Moreover, the crystals grown in dark maintained their original yellow color when exposed to light after their growth. On tracking the crystallization process, we noticed that the Black crystals are initially lighter in color and turn darker over time (3 or 4 days) as shown in Figures 1d-f.

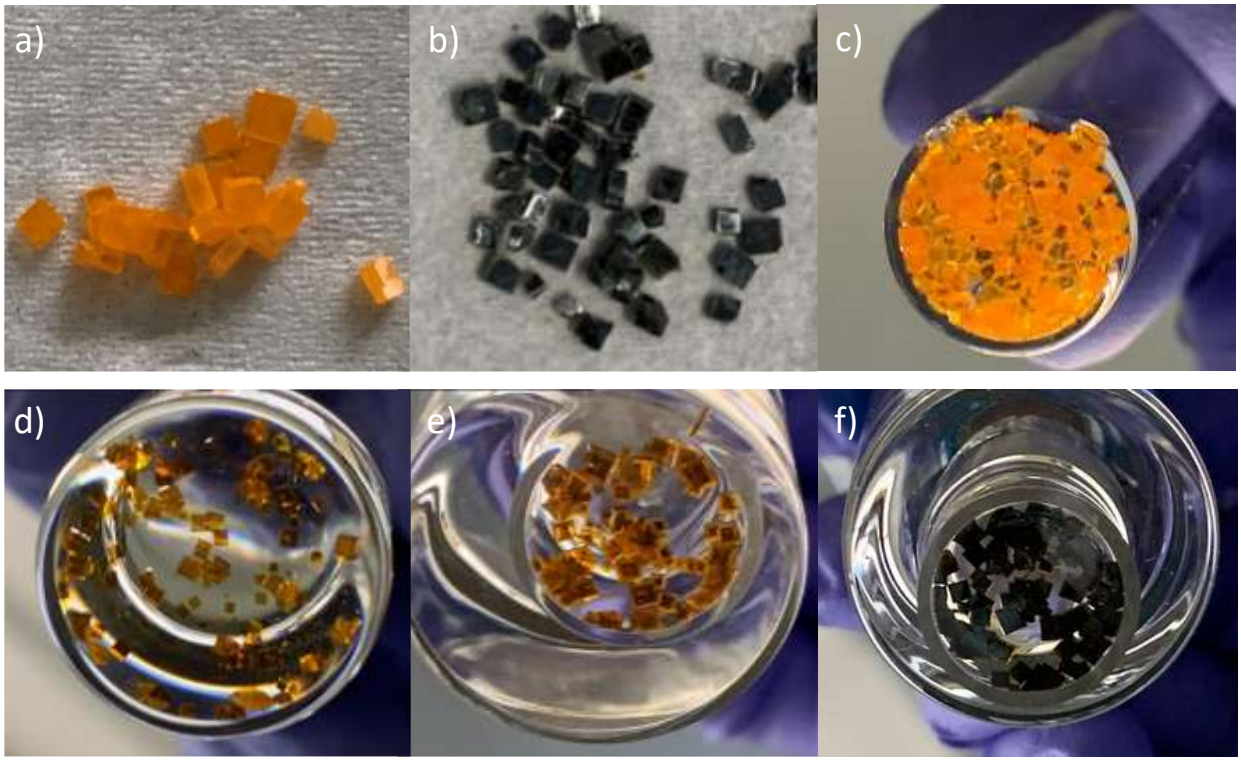

Figure 1. Photographs of (a) $DMA/MAPbBr_3$ crystals grown using low $PbBr_2$ concentration (0.4 M), (b) $DMA/MAPbBr_3$ crystals grown using high $PbBr_2$ concentration (1.2 M), (c) $DMA/MAPbBr_3$ crystals grown using high $PbBr_2$ concentration (1.2 M) but in dark conditions after 4 days of growth, and (d-f) $DMA/MAPbBr_3$ crystals grown using high $PbBr_2$ concentration (1.2 M) in ambient light conditions, showing color evolution of the crystals: (d) 1 day, (e) 1.5-2 days, and (f)

3-4 days. Note, photographs shown in Figure 1b and 1f are of crystals grown using high $PbBr_2$ concentration (1.2 M) after 4 days of growth, after and before collection of crystals, respectively.

Next, we performed compositional analysis of the Black crystals grown from the 1.2 M $PbBr_2$ solution while using the Yellow crystals grown from the 0.4 M $PbBr_2$ solution as our control sample. The results are summarized in Table 1. Liquid-state proton nuclear magnetic resonance (^{1}H NMR) analysis (Figure S2 in the Supporting Information) indicated that the DMA% in the Black crystals is very close to what we previously found in the Yellow crystals (around 44%).[16] The Br/Pb ratio, in both crystals, is maintained around 2.8, as determined from scanning electron microscopy-energy dispersive X-ray spectroscopy (SEM-EDS). Halide perovskites are usually reported as slightly halide-deficient, which could hint toward the formation of metallic lead.[17,18] X-ray photoelectron spectroscopy (XPS) in Figure S3 (in the Supporting Information) showed that, while there was an amount of metallic lead detected in both crystals, the Black crystals had a higher percentage of Pb(0) (5.5% of the total Pb content – that is more than double what was detected for the Yellow crystals) and it appears as a plausible source for the change in color. The opaque and metallic appearance of $MAPbBr_3$ crystals has been previously reported to occur, however, upon X-ray irradiation, and was similarly attributed to the formation of Pb(0).[19] Furthermore, the photoinduced formation of Pb(0) in the presence of excess PbX_2 was previously demonstrated by different research groups.[9,20–22] Surprisingly, our Black crystals were completely soluble in DMF leaving no black residue, unlike in the case of $FAPbBr_3$ crystals (FA = formamidinium), in which Wei *et al.*[23] observed a small amount of black material within the crystal that was collected upon the dissolution of the crystals in DMF and was identified as Pb(0) by XRD. Nevertheless, we cannot exclude that in case of our Black crystals, the detected Pb(0)

could be in the form of homogenously distributed tiny clusters that could influence the color of the crystals while not being easily isolated or detected by XRD[24] (i.e., the most intense diffraction peak ascribable to the Pb(0) phase identified by Wei et al.[23] was absent in the diffraction pattern of our Black crystals as described below).

Interestingly, when the Black crystals were cleaved, they still maintained a shiny black color in their core (Figure S4a in the Supporting Information); however, we observed a change in color from black to yellow upon grinding such Black crystals (Figure S4b). From XPS, we recorded a reduction in the Pb(0) content as it dropped from 5.5% in the as-grown Black crystals to 1.2% in the corresponding yellow-colored ground powders. As indicated in previous works, the photo-induced Pb(0) can reconvert to perovskite by reacting with MAX from the perovskite bulk.[25,26] Therefore, we ascribe the black coloring in the as-grown Black crystals to be due to Pb(0) that can convert into perovskite upon grinding.

In general, it is proposed that light-induced Pb(0) formation is due to the degradation of $MAPbX_3$ either directly into Pb(0) or into PbX_2 followed by its decomposition into Pb(0).[27,28] The formation of metallic lead in our Black crystals is possibly attributed to a combined MA and DMA photocatalyzed reduction of Pb(II) to Pb(0). This is corroborated not only by our results, in which we observed that for a single organic compound (either MA or DMA) no blackening occurred, but also by previously reported results suggesting that in the presence of MA only the reduction of Pb(II) to Pb(0) would be very slow.[20] The first stage after the reduction of Pb(II) to Pb(0) involves the formation of Pb(0) clusters with epitaxial relationship with the parent perovskite.[29] Such Pb(0) clusters survive up to a critical size after which they will rearrange losing their epitaxial

relationship with the surrounding perovskite. Furthermore, the growth of the Pb(0) clusters beyond that size leads to the formation of voids within the perovskite structure, thus degrading the parent perovskite. In our Black crystals, we propose that the formed Pb(0) clusters in the black-colored crystals do not grow large enough to be isolated upon dissolution in DMF or to degrade the crystallinity of the Black crystals. In fact, the crystallinity of the Black crystals was found to be even higher than the Yellow crystals as described in next sections.

Table 1. Elemental composition of Yellow and Black crystals.

Ratio	**Yellow Crystal**	**Black Crystal**
%DMA/(DMA+MA) (Liquid-state ^{1}H NMR)	44.0[16]	43.8
Br/Pb (EDS)	2.8	2.8
$\%[Pb^{0}]/[Pb]_{TOT}$ (XPS)	2.5	5.5

Other reported origins for color darkening in metal halide perovskites include the formation of localized mid-bandgap states due to the presence of mixed valence cations[30,31] or to the formation of color centers such as Pb^{3+},[32] and the induced formation of mid-bandgap defects related to disruption of the crystalline order[33] or to strain.[34] In our Black crystals, we excluded all these origins through detailed characterization as we describe next. Firstly, our XPS results indicate that the only difference between the Black and Yellow crystals is the increased Pb(0) in the Black crystals as discussed above. In addition, it appears that the valence band maxima (VBM) of the Black and Yellow crystals are both at 1.7 eV below the Fermi level (Figure S5 in the Supporting Information). Furthermore, we performed electron paramagnetic resonance

(EPR) measurements (not shown) and confirmed the absence of any EPR signal in the Black crystals both at room temperature and at liquid helium temperatures. Therefore, the black color cannot be due to the presence of mixed valence cations,[30,31] and/or formation of color centers.[32]

The laboratory X-ray powder diffraction (LXRPD) pattern of the as-grown Black crystals is similar to the Yellow crystals pattern, and matches the cubic 3D perovskite structure with no diffraction peaks belonging to the $DMAPbBr_3$ phase (Figure 2a). Zooming into the diffraction patterns, however, shows that the Black crystals have peaks that are shifted to lower Bragg angles compared to the Yellow crystals (Figure 2b). This cannot be explained by higher DMA incorporation levels in the Black crystals, as both crystals have very similar DMA/MA ratios as mentioned above. Instead, it could be attributed to the Yellow crystals being structurally compressed, as we reported previously.[16] When we carried out X-ray rocking curve (omega scan) measurements (Figure 2c) on the as-grown crystals, we obtained a significantly narrowed full width at half maximum (FWHM) of 0.014° in the case of the (004) peak for the Black crystals, compared to 0.18° for the Yellow crystals, indicating that the Black ones have a much enhanced crystallinity due to reduced density of dislocations and preferred orientation of crystallites.[35–38] This allows excluding color darkening to be a result of induced mid-bandgap defects due to disruption of the crystalline order, as previously reported for Bi-doped $MAPbBr_3$ single crystals.[33,39] The LXRPD patterns of both as-grown Black crystals and their powders (yellow in color) are identical in terms of peaks position (Figure S6a in the Supporting Information), therefore we can exclude strain as a cause of the unexpected change in color.[34]

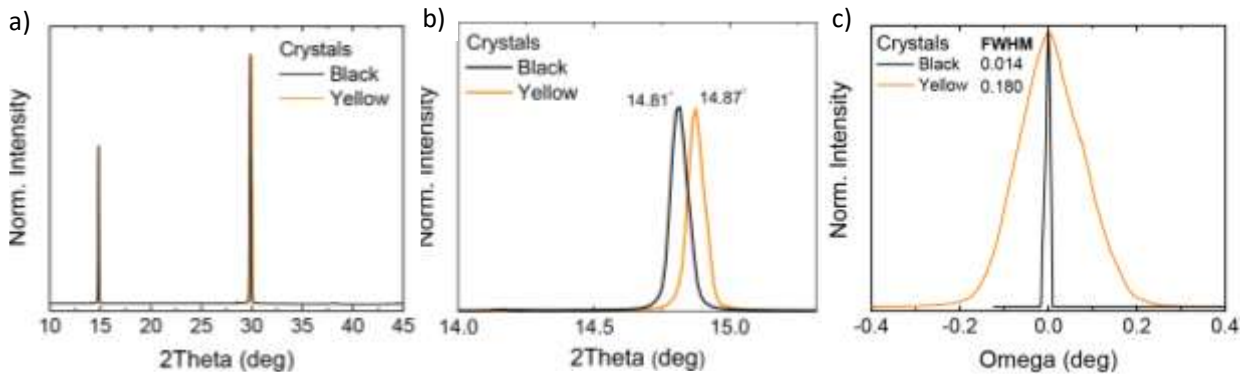

Figure 2. (a) LXRPD patterns of Black and Yellow crystals and (b) corresponding zoomed-in (001) peak of both crystals. (c) XRD rocking curve (Omega scan) of the (004) diffraction peaks of both Black and Yellow crystals.

The higher crystallinity of the Black crystals compared to the Yellow ones was also reflected in their powders when we carried out synchrotron X-ray powder diffraction (SXRPD) measurements. We observed that the diffraction peaks in the powder patterns from the Black crystals are about 5 times more intense compared to those in the powder patterns from the Yellow crystals (Figure S6b). On the powdered crystals, we also carried out temperature-dependent synchrotron XRD measurements and observed that the powders obtained from the Black crystals behave very similarly to those obtained from the Yellow crystals.[16] Both samples undergo a cubic to tetragonal phase transition at ~205 K, and no orthorhombic phase is observed down to 80 K (Table S1 in the Supporting Information). In the case of the powder obtained from the Black crystals, the *ab-initio* structure solution process by SXRPD data gave very similar results to those ones obtained by Yellow powders (i.e., no relevant changes in the perovskite crystal structure was observed).

We carried out further structural characterization to identify any possible differences between the Black and Yellow crystals. Micro-Raman spectroscopy carried out at room temperature shows that there are no significant differences in the organic cations (MA and DMA) vibration modes in terms of peak position and linewidth when comparing the Black and Yellow crystals, as well as in the Black crystals and their corresponding powders (Figure S7 in the Supporting Information). Moreover, when comparing Raman spectra of the Black and Yellow crystals with that of the pure $MAPbBr_3$ crystals, we confirmed the presence of the DMA cations in the Black and Yellow crystals with the appearance of the bands corresponding to C-N-C stretching, CH_3 rocking, and CH_3 bending modes of the DMA cation at 890, 1350 and 1461 cm^{-1}, respectively.[40,41] Interestingly, the N-H asymmetric bending mode (NH_3^+ in MA) is redshifted from 1589 cm^{-1} for $MAPbBr_3$ to ~1580 cm^{-1} in the mixed DMA/$MAPbBr_3$ crystals, demonstrating a stronger $H_N\cdots Br$ bonding for the MA cation in the mixed crystals than in the crystals formed of only MA (Figure S8 in the Supporting Information).[16,42] In terms of phase transitions, temperature-dependent micro-Raman measurements (Figures S9-11 in the Supporting Information) confirm the absence of an orthorhombic phase in the Black crystals, similar to what we reported in our previous work on the Yellow crystals,[16] since most of the MA modes such as C-H, N-H and C-N stretching and rocking modes show frequency and linewidth values comparable with the tetragonal phase of $MAPbBr_3$ down to 93 K (Table S2 in the Supporting Information). Moreover, we observed a change in the molecular vibration modes at ~205 K, in accordance with the cubic-to-tetragonal phase transition determined by XRD.

Through ^{207}Pb MAS solid-state NMR (SSNMR), as shown in Figure 3a, we found that there is a significant chemical shift difference ($\Delta\delta$ = 47 ppm) in the Black crystals spectrum (δ = 552

ppm) with respect to the Yellow crystals (δ = 505 ppm), suggesting that the local Pb environment in the two samples is different. The ^{207}Pb MAS SSNMR signal of the powders, obtained from grinding the Black crystals, shifts closer to the values obtained for the Yellow crystals and their powders. On the other hand, the ^{13}C and ^{1}H SSNMR signals are coincident for all samples, with no significant shifts or significant change in their FWHM (Figure S12 in the Supporting Information), in agreement with micro-Raman spectroscopy data.

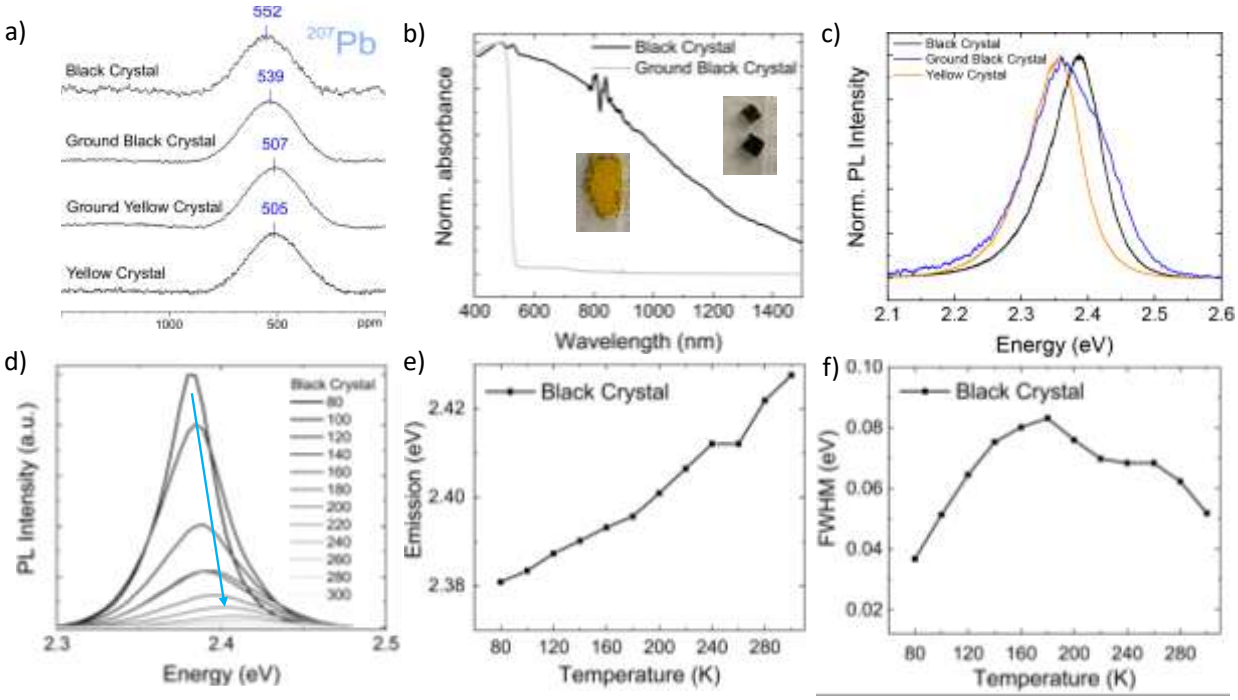

Figure 3. (a) ^{207}Pb (83.73 MHz) MAS SSNMR spectra of the Black and Yellow crystals and their respective powders, acquired at 10 kHz at room temperature. (b) Absorption of Black crystal in transmission geometry and the band edge absorption profile for their powder calculated from their diffuse reflectance spectra using the empirical Kubelka-Munk function[43,44] (the fluctuation in the spectra is due to a detector change) (c) Micro-photoluminescence spectra, measured with a micro-Raman spectrometer (457 nm excitation – 2.71 eV), of Black crystal and its powders

compared to Yellow crystal (d) Temperature-dependent PL spectra of the Black crystals using 445 nm (2.79 eV) excitation. Temperature-dependent evolution of (e) the peak position, and (f) FWHM of the Black crystals.

Then we turned our attention to the investigation of the influence of the black coloring and the presence of metallic lead on the optical properties of the Black crystals and their powders. The Black crystals show absorbance extending to the near-IR (Figure 3b). Such sub-bandgap absorption was previously attributed to metallic lead.[21] On powdering the Black crystals, in line with the disappearance of the black color, we observed loss of absorbance in the Vis-IR region (600-1300 nm). Micro-photoluminescence (PL) measurements (Figure 3c) carried out at room temperature showed that the emission from the powders of the Black crystals slightly red-shifts from 518 ± 3 nm for the as-grown Black crystals, to 523 ± 3 nm in powders, approaching the PL emission from the as-grown Yellow crystals 526 ± 2 nm (Figure 3d). Note that we also carried out infrared emission measurements on the as-grown Black crystals but did not detect any emission. This indicates no changes in the perovskite bandgap in the Black crystals. Instead, as suggested, the black coloring could be due to a small impurity that does not get integrated in the perovskite structure, such as Pb(0).

We next performed temperature-dependent PL measurements on the as-grown Black crystals (Figure 3d) and fit the peaks with a Voigt profile. Focusing on the emission maxima, the crystals showed a sequential blue shift (Figure 3e) throughout the increasing temperature range, in line with previous reports in literature, attributing such a shift to lattice thermal expansion and stabilization of the VBM.[45–48] Temperature-dependent emission FWHM broadening has been

used to define the dominant mechanisms of electron–phonon coupling, and in the case of $MAPbBr_3$ and $FAPbBr_3$ crystals the broadening was suggested to be due to Fröhlich interaction with optical phonons.[49] Interestingly, in the case of our Black crystals, the FWHM (Figure 3f) ceases to increase above 180–200 K, as possibly an additional temperature-activated process is reducing the electron-phonon coupling when approaching room temperature. Such behavior is not observed in the powders obtained from the Black crystals.

Finally, we fabricated vertical metal/semiconductor/metal devices with gold (Au) electrodes and studied their electrical performance. The photocurrent spectra (Figure 4a) confirmed that the bandgap of the Black crystals is in the visible region, similar to what we recorded from the μ-PL measurements of the Black crystals (Figure 3c). Furthermore, the photocurrent spectra of the Black crystal devices appear blue-shifted with respect to the ones of the Yellow crystals, in line with the blue shift observed from μ-PL. Once more, this highlights that the black coloring is most likely not due to a change in the bandgap of the perovskite crystals. Despite the higher metallic lead content, the higher crystalline quality of the Black crystals compared to the Yellow ones was also confirmed from their lower dark current (Figure 4b), indicating fewer defects, which is in agreement with their rocking curve measurements discussed above (Figure 2c).[14,50,51] Furthermore, we recorded suppressed hysteresis in the Black crystals (Figure 4b), which indicates reduced ion migration.[52]

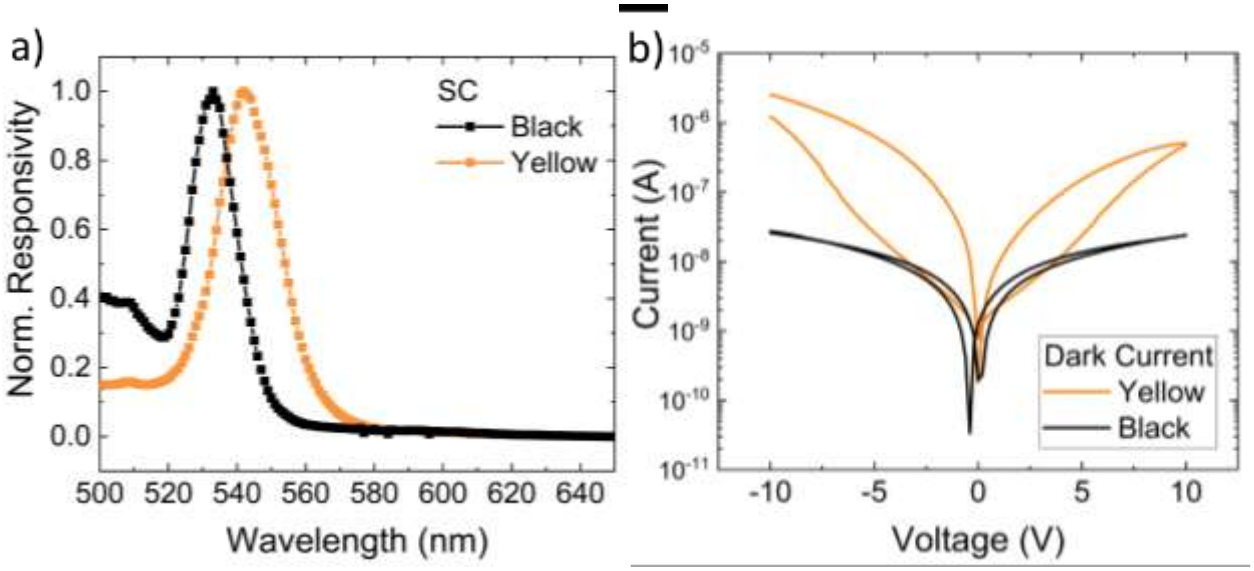

Figure 4. (a) Normalized spectral response of vertical metal/semiconductor/metal devices. (b) IV curves under dark conditions for both Yellow and Black crystal devices.

Conclusions

We grew black-looking mixed DMA/MAPbBr$_3$ crystals which contained more than double the Pb(0) detected in the typical yellow-colored DMA/MAPbBr$_3$ crystals. Nevertheless, the Black crystals are of a higher crystalline quality, as derived by X-ray rocking curve measurements. Furthermore, the lower dark current measured in the case of the Black crystals compared to the Yellow ones indicated fewer defects in the Black crystals. However, the apparent black color of these Br-based crystals was not reflected in their PL and their spectral photocurrent response. Instead, PL and photocurrent spectra matched what is expected from a material with a bandgap of around 2.3–2.4 eV. This confirms that the black color is not related to a change in the lead bromide perovskite bandgap, but due to the presence of a small amount of localized impurities, which is likely represented by tiny lead clusters. Our results highlight the importance of

understanding the halide perovskite precursor solution chemistry and reveals that the precursor solution can facilitate the formation of metallic lead during the crystallization process. This is of critical importance as in many cases halide perovskites for optoelectronic devices are deposited from a DMF solution[25,53,54] that can result in unintentional incorporation of the DMA cations in the perovskite material,[55,56] which in the presence of the MA cations can facilitate the formation of metallic lead as we demonstrate here.

Acknowledgements

B.M.G. thanks the funding support from the Spanish MCIN/AEI under Projects PID2019-108153GA-I00 & PID2021-128004NB-C21 and Ramón y Cajal Fellowship, Gipuzkoa Council (Spain) in the frame of Gipuzkoa Fellows Program, and Basque Science Foundation for Science (IKERBASQUE) with HYMNOS project in the frame of Research Fellows Program. Dr. F. Balsassarre and R. Lassandro are acknowledged for their technical assistance and Dr. C. Chiarella and Dr. L. Cassano for their administrative support.

Supporting Information

LXRPD patterns and photographs of crystals grown from different DMA:MA ratios; liquid-state ^{1}H NMR of the Black crystals; XPS spectra of both Yellow and Black crystals; photographs of cleaved surface and ground powder of a Black DMA/MAPbBr$_3$ crystal; Raman spectra of both Yellow and Black crystals; temperature-dependent SPXRD data of the ground powder of a Black DMA/MAPbBr$_3$ crystal; ^{13}C (100.64 MHz) CPMAS (left) and ^{1}H (400.23 MHz) MAS (right) SSNMR spectra of Black and Yellow crystals and their corresponding powders

References

(1) Yoo, J. J.; Shin, S. S.; Seo, J. Toward Efficient Perovskite Solar Cells: Progress, Strategies, and Perspectives. *ACS Energy Lett.* **2022**, *7*, 2084–2091.

(2) Tan, Z.; Li, J.; Zhang, C.; Li, Z.; Hu, Q.; Xiao, Z.; Kamiya, T.; Hosono, H.; Niu, G.; Lifshitz, E.; Cheng, Y.; Tang, J. Highly Efficient Blue-Emitting Bi-Doped Cs_2SnCl_6 Perovskite Variant: Photoluminescence Induced by Impurity Doping. *Adv. Funct. Mater.* **2018**, *28*, 1801131.

(3) Wang, L.; Zhou, H.; Hu, J.; Huang, B.; Sun, M.; Dong, B.; Zheng, G.; Huang, Y.; Chen, Y.; Li, L.; Xu, Z.; Li, N.; Liu, Z.; Chen, Q.; Sun, L. D.; Yan, C. H. A Eu^{3+}-Eu^{2+} Ion Redox Shuttle Imparts Operational Durability to Pb-I Perovskite Solar Cells. *Science* **2019**, *363*, 265–270.

(4) Akbulatov, A. F.; Frolova, L. A.; Dremova, N. N.; Zhidkov, I.; Martynenko, V. M.; Tsarev, S. A.; Luchkin, S. Y.; Kurmaev, E. Z.; Aldoshin, S. M.; Stevenson, K. J.; Troshin, P. A. Light or Heat: What Is Killing Lead Halide Perovskites under Solar Cell Operation Conditions? *J. Phys. Chem. Lett.* **2020**, *11*, 333–339.

(5) Zhang, W.; Pathak, S.; Sakai, N.; Stergiopoulos, T.; Nayak, P. K.; Noel, N. K.; Haghighirad, A. A.; Burlakov, V. M.; Dequilettes, D. W.; Sadhanala, A.; Li, W.; Wang, L.; Ginger, D. S.; Friend, R. H.; Snaith, H. J. Enhanced Optoelectronic Quality of Perovskite Thin Films with Hypophosphorous Acid for Planar Heterojunction Solar Cells. *Nat. Commun.* **2015**, *6*, 1–9.

(6) Ren, Z.; Yu, J.; Qin, Z.; Wang, J.; Sun, J.; Chan, C. C. S.; Ding, S.; Wang, K.; Chen, R.; Wong, K. S.; Lu, X.; Yin, W. J.; Choy, W. C. H. High-Performance Blue Perovskite Light-Emitting Diodes Enabled by Efficient Energy Transfer between Coupled Quasi-2D Perovskite

Layers. *Adv. Mater.* **2021**, *33*, 2005570.

(7) Xiao, Z.; Kerner, R. A.; Zhao, L.; Tran, N. L.; Lee, K. M.; Koh, T. W.; Scholes, G. D.; Rand, B. P. Efficient Perovskite Light-Emitting Diodes Featuring Nanometre-Sized Crystallites. *Nat. Photonics* **2017**, *11*, 108–115.

(8) Cho, H.; Jeong, S. H.; Park, M. H.; Kim, Y. H.; Wolf, C.; Lee, C. L.; Heo, J. H.; Sadhanala, A.; Myoung, N. S.; Yoo, S.; Im, S. H.; Friend, R. H.; Lee, T. W. Overcoming the Electroluminescence Efficiency Limitations of Perovskite Light-Emitting Diodes. *Science* **2015**, *350*, 1222–1225.

(9) Liang, J.; Hu, X.; Wang, C.; Liang, C.; Chen, C.; Xiao, M.; Li, J.; Tao, C.; Xing, G.; Yu, R.; Ke, W.; Fang, G. Origins and Influences of Metallic Lead in Perovskite Solar Cells. *Joule* **2022**, *6*, 816–833.

(10) Wu, P. S. C.; Otting, G. Rapid Pulse Length Determination in High-Resolution NMR. *J. Magn. Reson.* **2005**, *176*, 115–119.

(11) Degen, T.; Sadki, M.; Bron, E.; König, U.; Nénert, G. The High Score Suite. In *Powder Diffraction*; Cambridge University Press, **2014**; 29, S13–S18.

(12) Willmott, P. R.; Meister, D.; Leake, S. J.; Lange, M.; Bergamaschi, A.; Böge, M.; Calvi, M.; Cancellieri, C.; Casati, N.; Cervellino, A.; Chen, Q.; David, C.; Flechsig, U.; Gozzo, F.; Henrich, B.; Jäggi-Spielmann, S.; Jakob, B.; Kalichava, I.; Karvinen, P.; Krempasky, J.; Lüdeke, A.; Lüscher, R.; Maag, S.; Quitmann, C.; Reinle-Schmitt, M. L.; Schmidt, T.; Schmitt, B.; Streun, A.; Vartiainen, I.; Vitins, M.; Wang, X.; Wullschleger, R. The Materials

Science Beamline Upgrade at the Swiss Light Source. *J. Synchrotron Radiat.* **2013**, *20*, 667.

(13) Shamsi, J.; Abdelhady, A. L.; Accornero, S.; Arciniegas, M.; Goldoni, L.; Kandada, A. R. S.; Petrozza, A.; Manna, L. N -Methylformamide as a Source of Methylammonium Ions in the Synthesis of Lead Halide Perovskite Nanocrystals and Bulk Crystals. *ACS Energy Lett.* **2016**, *1*, 1042–1048.

(14) Boopathi, K. M.; Martín-García, B.; Ray, A.; Pina, J. M.; Marras, S.; Saidaminov, M. I.; Bonaccorso, F.; Di Stasio, F.; Sargent, E. H.; Manna, L.; Abdelhady, A. L.; Pina, M.; Marras, S.; Saidaminov, M. I.; Bonaccorso, F.; Stasio, F. Di; Sargent, E. H.; Manna, L.; Abdelhady, A. L. Permanent Lattice Compression of Lead-Halide Perovskite for Persistently Enhanced Optoelectronic Properties. *ACS Energy Lett.* **2020**, *5*, 642–649.

(15) Ray, A.; Martín-García, B.; Martinelli, A.; Spirito, D.; Locardi, F.; Altamura, D.; Giannini, C.; Prato, M.; Manna, L.; Abdelhady, A. L. Impact of Local Structure on Halogen Ion Migration in Layered Methylammonium Copper Halide Memory Devices. *J. Mater. Chem. A* **2020**, *8*, 17516–17526.

(16) Ray, A.; Martín-García, B.; Moliterni, A.; Casati, N.; Boopathi, K. M.; Spirito, D.; Goldoni, L.; Prato, M.; Giacobbe, C.; Giannini, C.; Stasio, F. Di; Krahne, R.; Manna, L.; Abdelhady, A. L. Mixed Dimethylammonium/Methylammonium Lead Halide Perovskite Single Crystals for Improved Structural Stability and Enhanced Photodetection. *Adv. Mater.* **2021**, *7*, 2106160.

(17) Lindblad, R.; Jena, N. K.; Philippe, B.; Oscarsson, J.; Bi, D.; Lindblad, A.; Mandal, S.; Pal, B.; Sarma, D. D.; Karis, O.; Siegbahn, H.; Johansson, E. M. J.; Odelius, M.; Rensmo, H. Electronic Structure of $CH_3NH_3PbX_3$ Perovskites: Dependence on the Halide Moiety. *J. Phys. Chem. C* **2015**, *119*, 1818–1825.

(18) Lindblad, R.; Bi, D.; Park, B. W.; Oscarsson, J.; Gorgoi, M.; Siegbahn, H.; Odelius, M.; Johansson, E. M. J.; Rensmo, H. Electronic Structure of $TiO_2/CH_3NH_3PbI_3$ Perovskite Solar Cell Interfaces. *J. Phys. Chem. Lett.* **2014**, *5*, 648–653.

(19) Ecker, B. R.; Wang, C.; Wei, H.; Yuan, Y.; Huang, J.; Gao, Y. Intrinsic Behavior of $CH_3NH_3PbBr_3$ Single Crystals under Light Illumination. *Adv. Mater. Interfaces* **2018**, *5*, 1801206.

(20) Hu, J.; Kerner, R. A.; Pelczer, I.; Rand, B. P.; Schwartz, J. Organoammonium-Ion-Based Perovskites Can Degrade to Pb^0 via Amine-Pb(II) Coordination. *ACS Energy Lett.* **2021**, *6*, 2262–2267.

(21) Holovský, J.; Peter Amalathas, A.; Landová, L.; Dzurňák, B.; Conrad, B.; Ledinský, M.; Hájková, Z.; Pop-Georgievski, O.; Svoboda, J.; Yang, T. C. J.; Jeangros, Q. Lead Halide Residue as a Source of Light-Induced Reversible Defects in Hybrid Perovskite Layers and Solar Cells. *ACS Energy Lett.* **2019**, *4*, 3011–3017.

(22) Roose, B.; Dey, K.; Chiang, Y.-H.; Friend, R. H.; Stranks, S. D. Critical Assessment of the Use of Excess Lead Iodide in Lead Halide Perovskite Solar Cells. *J. Phys. Chem. Lett.* **2020**, *11*, 6505–6512.

(23) Wei, H.; Chen, S.; Zhao, J.; Yu, Z.; Huang, J. Is Formamidinium Always More Stable than Methylammonium? *Chem. Mater.* **2020**, *32*, 2501–2507.

(24) Alberti, A.; Bongiorno, C.; Smecca, E.; Deretzis, I.; La Magna, A.; Spinella, C. Pb Clustering and PbI_2 Nanofragmentation during Methylammonium Lead Iodide Perovskite Degradation. *Nat. Commun.* **2019**, *10*, 1–11.

(25) Cappel, U. B.; Svanström, S.; Lanzilotto, V.; Johansson, F. O. L.; Aitola, K.; Philippe, B.; Giangrisostomi, E.; Ovsyannikov, R.; Leitner, T.; Föhlisch, A.; Svensson, S.; Mårtensson, N.; Boschloo, G.; Lindblad, A.; Rensmo, H. Partially Reversible Photoinduced Chemical Changes in a Mixed-Ion Perovskite Material for Solar Cells. *ACS Appl. Mater. Interfaces* **2017**, *9*, 34970–34978.

(26) Zhang, Y.; Kim, D.; Yun, J. H.; Lim, J.; Jung, M. C.; Wen, X.; Seidel, J.; Choi, E.; Xiao, M.; Qiu, T.; Lyu, M.; Han, E. Q.; Ghasemi, M.; Lim, S.; Snaith, H. J.; Yun, J. S.; Wang, L. Self-Assembled Perovskite Nanoislands on $CH_3NH_3PbI_3$ Cuboid Single Crystals by Energetic Surface Engineering. *Adv. Funct. Mater.* **2021**, *31*, 2105542.

(27) Kerner, R. A.; Schloemer, T. H.; Schulz, P.; Berry, J. J.; Schwartz, J.; Sellinger, A.; Rand, B. P. Amine Additive Reactions Induced by the Soft Lewis Acidity of Pb^{2+} in Halide Perovskites. Part I: Evidence for Pb–Alkylamide Formation. *J. Mater. Chem. C* **2019**, *7*, 5251–5259.

(28) Tang, X.; Brandl, M.; May, B.; Levchuk, I.; Hou, Y.; Richter, M.; Chen, H.; Chen, S.; Kahmann, S.; Osvet, A.; Maier, F.; Steinrück, H. P.; Hock, R.; Matt, G. J.; Brabec, C. J.

Photoinduced Degradation of Methylammonium Lead Triiodide Perovskite Semiconductors. *J. Mater. Chem. A* **2016**, *4*, 15896–15903.

(29) Dang, Z.; Shamsi, J.; Palazon, F.; Imran, M.; Akkerman, Q. A.; Park, S.; Bertoni, G.; Prato, M.; Brescia, R.; Manna, L. In Situ Transmission Electron Microscopy Study of Electron Beam-Induced Transformations in Colloidal Cesium Lead Halide Perovskite Nanocrystals. **2017**, *11*, 2124–2132.

(30) Krajewska, C. J.; Kavanagh, S. R.; Zhang, L.; Kubicki, D. J.; Dey, K.; Gałkowski, K.; Grey, C. P.; Stranks, S. D.; Walsh, A.; Scanlon, D. O.; Palgrave, R. G. Enhanced Visible Light Absorption in Layered $Cs_3Bi_2Br_9$ through Mixed-Valence Sn(II)/Sn(IV) Doping. *Chem. Sci.* **2021**, *12*, 14686–14699.

(31) Wei, F.; Deng, Z.; Sun, S.; Hartono, N. T. P.; Seng, H. L.; Buonassisi, T.; Bristowe, P. D.; Cheetham, A. K. Enhanced Visible Light Absorption for Lead-Free Double Perovskite $Cs_2AgSbBr_6$. *Chem. Commun.* **2019**, *55*, 3721–3724.

(32) Shkrob, I. A.; Marin, T. W. Charge Trapping in Photovoltaically Active Perovskites and Related Halogenoplumbate Compounds. *J. Phys. Chem. Lett.* **2014**, *5*, 1066–1071.

(33) Nayak, P. K.; Sendner, M.; Wenger, B.; Wang, Z.; Sharma, K.; Ramadan, A. J.; Lovrinčić, R.; Pucci, A.; Madhu, P. K.; Snaith, H. J. Impact of Bi3+ Heterovalent Doping in Organic-Inorganic Metal Halide Perovskite Crystals. *J. Am. Chem. Soc.* **2018**, *140*, 574–577.

(34) Singh, A.; Chaurasiya, R.; Bheemaraju, A.; Chen, J. S.; Satapathi, S. Strain-Induced Band-Edge Modulation in Lead-Free Antimony-Based Double Perovskite for Visible-Light

Absorption. *ACS Appl. Energy Mater.* **2022**, *5*, 3926–3932.

(35) Lian, Z.; Yan, Q.; Gao, T.; Ding, J.; Lv, Q.; Ning, C.; Li, Q.; Sun, J. Perovskite CH3NH3PbI3(Cl) Single Crystals: Rapid Solution Growth, Unparalleled Crystalline Quality, and Low Trap Density toward 108 Cm^{-3}. *J. Am. Chem. Soc.* **2016**, *138*, 9409–9412.

(36) Liu, Y.; Zhang, Y.; Yang, Z.; Feng, J.; Xu, Z.; Li, Q.; Hu, M.; Ye, H.; Zhang, X.; Liu, M.; Zhao, K.; Liu, S. Low-Temperature-Gradient Crystallization for Multi-Inch High-Quality Perovskite Single Crystals for Record Performance Photodetectors. *Mater. Today* **2019**, *22*, 67–75.

(37) Wang, W.; Meng, H.; Qi, H.; Xu, H.; Du, W.; Yang, Y.; Yi, Y.; Jing, S.; Xu, S.; Hong, F.; Qin, J.; Huang, J.; Xu, Z.; Zhu, Y.; Xu, R.; Lai, J.; Xu, F.; Wang, L.; Zhu, J. Electronic-Grade High-Quality Perovskite Single Crystals by a Steady Self-Supply Solution Growth for High-Performance X-Ray Detectors. *Adv. Mater.* **2020**, *32*, 2001540.

(38) Xu, R.; Hong, Z.; Tong, X.; Wang, W.; Meng, H.; Qin, J.; Wang, X.; Shu, X.; Cai, J.; Zhang, Z.; Xu, F.; Xu, H.; Hong, F.; Qi, H.; Lai, J.; Li, D. Uncovering the Formation Mechanism of Striations and Pyramidal Pits on a Native $MAPbI_3$ Single-Crystal Surface. *J. Phys. Chem. C* **2022**, *126*, 7319–7325.

(39) Abdelhady, A. L.; Saidaminov, M. I.; Murali, B.; Adinolfi, V.; Voznyy, O.; Katsiev, K.; Alarousu, E.; Comin, R.; Dursun, I.; Sinatra, L.; Sargent, E. H.; Mohammed, O. F.; Bakr, O. M. Heterovalent Dopant Incorporation for Bandgap and Type Engineering of Perovskite Crystals. *J. Phys. Chem. Lett.* **2016**, *7*, 295–301.

(40) Mączka, M.; Ptak, M. Simple, Fast and Non-Destructive Method for Detection of Dimethylammonium Impurity in Photovoltaic Methylammonium Lead Halides. *Appl. solid state Chem.* **2018**, *1*, 45–48.

(41) Simenas, M.; Balciunas, S.; Wilson, J. N.; Svirskas, S.; Kinka, M.; Garbaras, A.; Kalendra, V.; Gagor, A.; Szewczyk, D.; Sieradzki, A.; Maczka, M.; Samulionis, V.; Walsh, A.; Grigalaitis, R.; Banys, J. Suppression of Phase Transitions and Glass Phase Signatures in Mixed Cation Halide Perovskites. *Nat. Commun.* **2020**, *11*, 1–9.

(42) Yin, T.; Fang, Y.; Fan, X.; Zhang, B.; Kuo, J. L.; White, T. J.; Chow, G. M.; Yan, J.; Shen, Z. X. Hydrogen-Bonding Evolution during the Polymorphic Transformations in $CH_3NH_3PbBr_3$: Experiment and Theory. *Chem. Mater.* **2017**, *29*, 5974–5981.

(43) Mancini, A.; Quadrelli, P.; Milanese, C.; Patrini, M.; Guizzetti, G.; Malavasi, L. $CH_3NH_3Sn_xPb_{1-x}Br_3$ Hybrid Perovskite Solid Solution: Synthesis, Structure, and Optical Properties. *Inorg. Chem.* **2015**, *54*, 8893–8895.

(44) Wu, B.; Nguyen, H. T.; Ku, Z.; Han, G.; Giovanni, D.; Mathews, N.; Fan, H. J.; Sum, T. C. Discerning the Surface and Bulk Recombination Kinetics of Organic–Inorganic Halide Perovskite Single Crystals. *Adv. Energy Mater.* **2016**, *6*, 1–9.

(45) Dar, M. I.; Jacopin, G.; Meloni, S.; Mattoni, A.; Arora, N.; Boziki, A.; Zakeeruddin, S. M.; Rothlisberger, U.; Grätzel, M. Origin of Unusual Bandgap Shift and Dual Emission in Organic-Inorganic Lead Halide Perovskites. *Sci. Adv.* **2016**, *2*, e1601156.

(46) Frost, J. M.; Butler, K. T.; Brivio, F.; Hendon, C. H.; Van Schilfgaarde, M.; Walsh, A.

Atomistic Origins of High-Performance in Hybrid Halide Perovskite Solar Cells. *Nano Lett.* **2014**, *14*, 2584–2590.

(47) Panzer, F.; Li, C.; Meier, T.; Köhler, A.; Huettner, S. Impact of Structural Dynamics on the Optical Properties of Methylammonium Lead Iodide Perovskites. *Adv. Energy Mater.* **2017**, *7*, 1700286.

(48) Francisco-López, A.; Charles, B.; Weber, O. J.; Alonso, M. I.; Garriga, M.; Campoy-Quiles, M.; Weller, M. T.; Goñi, A. R. Equal Footing of Thermal Expansion and Electron-Phonon Interaction in the Temperature Dependence of Lead Halide Perovskite Band Gaps. *J. Phys. Chem. Lett.* **2019**, *10*, 2971–2977.

(49) Wright, A. D.; Verdi, C.; Milot, R. L.; Eperon, G. E.; Pérez-Osorio, M. A.; Snaith, H. J.; Giustino, F.; Johnston, M. B.; Herz, L. M. Electron-Phonon Coupling in Hybrid Lead Halide Perovskites. *Nat. Commun.* **2016**, *7*, 1–9.

(50) Liu, Y.; Zhang, Y.; Yang, Z. Z.; Ye, H.; Feng, J.; Xu, Z.; Zhang, X.; Munir, R.; Liu, J.; Zuo, P.; Li, Q.; Hu, M.; Meng, L.; Wang, K.; Smilgies, D. M.; Zhao, G.; Xu, H.; Yang, Z. Z.; Amassian, A.; Li, J.; Zhao, K.; Liu, S. F. Multi-Inch Single-Crystalline Perovskite Membrane for High-Detectivity Flexible Photosensors. **2018**, *9*, 1–11.

(51) Ahmadi, M.; Wu, T.; Hu, B. A Review on Organic–Inorganic Halide Perovskite Photodetectors: Device Engineering and Fundamental Physics. *Adv. Mater.* **2017**, *29*, 1–24.

(52) Ferdani, D. W.; Pering, S. R.; Ghosh, D.; Kubiak, P.; Walker, A. B.; Lewis, S. E.; Johnson, A.

L.; Baker, P. J.; Islam, M. S.; Cameron, P. J. Partial Cation Substitution Reduces Iodide Ion Transport in Lead Iodide Perovskite Solar Cells. *Energy Environ. Sci.* **2019**, *12*, 2264–2272.

(53) Sadoughi, G.; Starr, D. E.; Handick, E.; Stranks, S. D.; Gorgoi, M.; Wilks, R. G.; Bär, M.; Snaith, H. J. Observation and Mediation of the Presence of Metallic Lead in Organic-Inorganic Perovskite Films. *ACS Appl. Mater. Interfaces* **2015**, *7*, 13440–13444.

(54) Alharbi, E. A.; Krishna, A.; Baumeler, T. P.; Dankl, M.; Fish, G. C.; Eickemeyer, F.; Ouellette, O.; Ahlawat, P.; Škorjanc, V.; John, E.; Yang, B.; Pfeifer, L.; Avalos, C. E.; Pan, L.; Mensi, M.; Schouwink, P. A.; Moser, J. E.; Hagfeldt, A.; Rothlisberger, U.; Zakeeruddin, S. M.; Grätzel, M. Methylammonium Triiodide for Defect Engineering of High-Efficiency Perovskite Solar Cells. *ACS Energy Lett.* **2021**, *6*, 3650–3660.

(55) Lee, M. V.; Raga, S. R.; Kato, Y.; Leyden, M. R.; Ono, L. K.; Wang, S.; Qi, Y. Transamidation of Dimethylformamide during Alkylammonium Lead Triiodide Film Formation for Perovskite Solar Cells. *J. Mater. Res.* **2017**, *32*, 45–55.

(56) Ke, W.; Spanopoulos, I.; Stoumpos, C. C.; Kanatzidis, M. G. Myths and Reality of HPbI3 in Halide Perovskite Solar Cells. *Nat. Commun.* **2018**, *9*, 1–9.

TOC

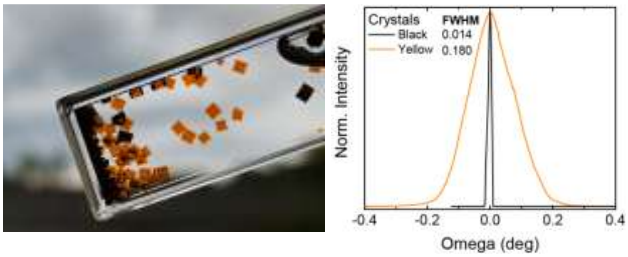
Crystals
Black
Yellow
FWHM
0.014
0.180
Norm. Intensity
-0.4
-0.2
0.0
0.2
0.4
Omega (deg)